# Recent Advances in the Operational Vicarious Calibration of Visible and Near-infrared Ocean Color Satellite Radiometry

P. Jeremy Werdell, Bryan A. Franz, Sean W. Bailey, and Charles R. McClain
NASA Goddard Space Flight Center ~ http://oceancolor.gsfc.nasa.gov

## INTRODUCTION

Satellite-borne ocean color sensors measure the visible (VIS) and near-infrared (NIR) radiance exiting the top of the atmosphere, $L_t(\lambda)$. Semi-analytical algorithms are used to retrieve the portion of $L_t(\lambda)$ that exits the sea surface, $L_w(\lambda)$, which accounts for ~10% of the total signal in the blue-green spectral regime. The $L_w(\lambda)$ are used in turn to estimate other geophysical parameters, such as the concentration of the phytoplankton pigment chlorophyll *a*, $C_a$, via the application of secondary bio-optical algorithms. The oceanographic community relies heavily on such data products to support studies ranging from managment of regional ecosystems to development of decadal climate records.

The desired uncertainties on $L_w(\lambda)$ cannot be achieved through pre-launch laboratory calibration and characterizations alone (Gordon 1988). The pre-launch calibration uncertainties for SeaWiFS, for example, are ~3% of $L_t(\lambda)$, which translates to relative uncertainties of ~30% for $L_w(\lambda)$ (Eplee et al. 2001), well above the mission goal of 5% for the retrieval of $L_w(443)$ in oligotrophic conditions. To retrieve sufficiently accurate $L_w(\lambda)$, ocean color sensors require additional on-orbit calibration. Here, we describe recent advances and outstanding issues in the NASA Ocean Biology Processing Group (OBPG) vicarious calibration approach for ocean color satellite visible and near-infrared radiometry.

The methodology described here does not presume anything about the heritage of the $L_{wn}$ targeted for calibration. While the OBPG uses $L_{wn}$ from the Marine Optical Buoy (MOBY; Clark et al. 1997) for the visible band calibration, the approach generically permits the use of $L_{wn}$ from regional climatologies, models, or another remote sensor.

## APPROACH

To describe the vicarious calibration process, it is useful to review the components of the atmospheric correction process (Gordon and Wang 1994), where $L_t(\lambda)$ and $L_w(\lambda)$ are the input and output, respectively:

$$L_t = \left(L_r + L_a + t_{dv}L_f + t_{dv}L_w\right)t_{gv}t_{gs}f_p \qquad (1)$$

The unknown terms in (1) are $L_w$, $L_a$, and $t_d$ (Table 1).

The $L_w$ are subsequently normalized to the scenario of a non-attenuating atmosphere with the Sun directly overhead at a distance of 1 AU:

$$L_{wn} = L_w\left(\mu_s t_{ds} f_s f_b f_\lambda\right)^{-1} \qquad (2)$$

The vicarious calibration process is effectively just an inversion of this forward processing algorithm, wherein known $L_{wn}$ provide the input and predicted $L_t$ become the output.

The ratio of predicted-to-observed $L_t$ is the vicarious gain, $g$: the correction factor that when applied to the observed $L_t$ forces the instrument-atmospheric correction system to yield the expected $L_{wn}$.

$$L^t_{wn} = L^t_w\left(\mu^t_s\, t^t_{ds}\, f^t_s\, f^t_b\, f^t_\lambda\right)^{-1} \qquad (3)$$

$$L^t_t = \left\{L_r + L_a + t_{dv}L_f + t_{dv}L^t_{wn}\left(\mu_s t_{ds} f_s f_b f_\lambda\right)\right\}t_{gv}t_{gs}f_p \qquad (4)$$

$$g = L^t_t\, L^{-1}_t \qquad (5)$$

The terms in (3) may differ from those in (2) because of differences in the solar and view path geometries between the target value of $L_w$, if, for example, the observations were collected at different times of day.

| Symbol | Description | Symbol | Description |
|---|---|---|---|
| $f_p$ | polarization correction factor | $L_f$ | radiance due to white caps and foam at the sea surface |
| $f_s$ | Earth-Sun distance correction factor | $L_w$ | water-leaving radiance |
| $f_\lambda$ | band-pass adjustment correction factor | $L_{wn}$ | normalized water-leaving radiance |
| $f_b$ | bidirectional reflectance correction factor | $s$ | subscript denoting solar path |
| $g$ | vicarious gain for a single observation | $t$ | superscript denoting a predicted value |
| $\overline{g}$ | mean vicarious gain for all observations | $t_g$ | transmittance due to gaseous absorption |
| $L_t$ | radiance observed at the top of the atmosphere | $t_d$ | Rayleigh-aerosol diffuse transmittance |
| $L_r$ | radiance due to Rayleigh scattering of air molecules | $v$ | subscript denoting sensor view path |
| $L_a$ | radiance due to scattering by aerosols | $\theta$ | cosine of zenith angle |

TABLE 1

The target $t_d$ is obtained either from target observations or derived from the satellite retrieval, the latter more advantageous in that it ensures that the $L_w$ are normalized with a common atmosphere.

Note that all terms in (1) are computed for the full relative spectral response of each sensor band. When required, $f_\lambda$ convert the full-band $L_{wn}$ to a nominal center wavelength, effectively removing residual out-of-band response. In the general case, $f_\lambda$ is used to shift $L_{wn}$ to the band-pass of the sensor to be calibrated.

## IMPLEMENTATION

We begin with the NIR calibration and two simplifying assumptions. First, that target sites exist where $L_w$(NIR) is negligible and the aerosol type is known. This reduces (1) and (4) and leaves $L_a$ as the only unknown term.

$$L_t = \left(L_r + L_a + t_{dv}L_f\right)t_{gv}t_{gs}f_p \qquad (6)$$

$$L^t_t = \left(L_r + L^t_a + t_{dv}L_f\right)t_{gv}t_{gs}f_p \qquad (7)$$

Second, we assume that the instrument calibration of the longer NIR band (e.g., 865-nm) is perfect, such that $g(865)$ is unity.

We then calibrate the shorter NIR band (e.g., 765-nm). The ratio of the two $L_a$(NIR) determines the aerosol type. As such, we use the known aerosol type and $L_a(865)$ to determine $L_a(765)$. Then, using (7) and (5), $L_t(765)$ can be predicted and compared with the observed $L_t(765)$ to generate $g(765)$.

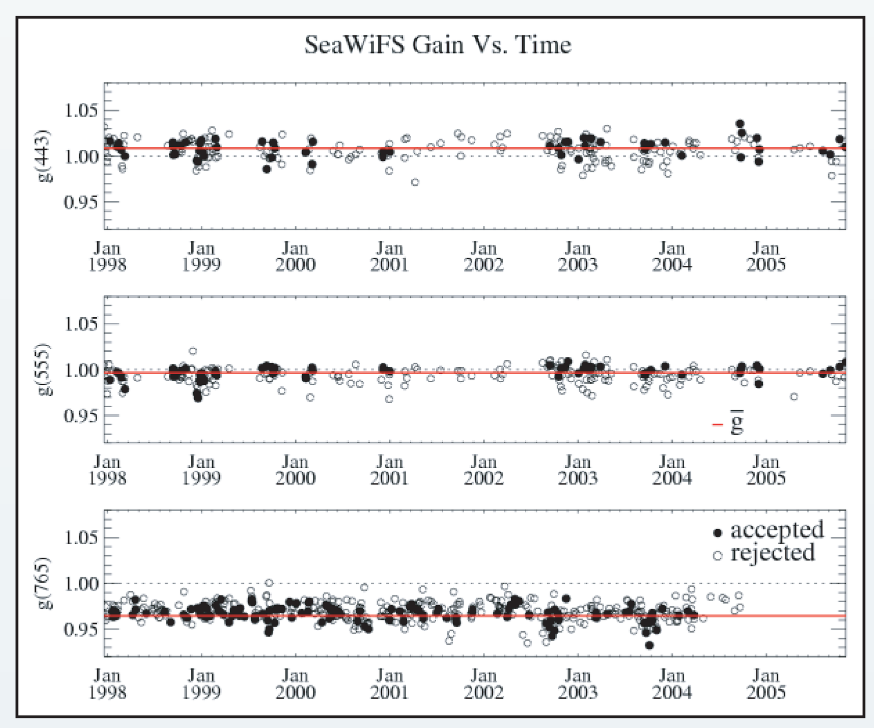


FIGURE 1

The process is completely independent of the VIS calibration, so the Earth location of the NIR calibration sites need not be coincident with those for the VIS bands. The OBPG currently uses two deep ocean sites for the NIR calibration, the South Pacific Gyre and the Southern Indian Ocean, with the maritime aerosol model at 90% humidity.

Once locations have been selected, cloud and glint-free observations are identified, and the fixed aerosol type is used to compute $g$ for each observation date. The individual $g$ are averaged to determine the mean vicarious gain, $\overline{g}$, for the shorter NIR band (Table 2, Figures 1 - 3).

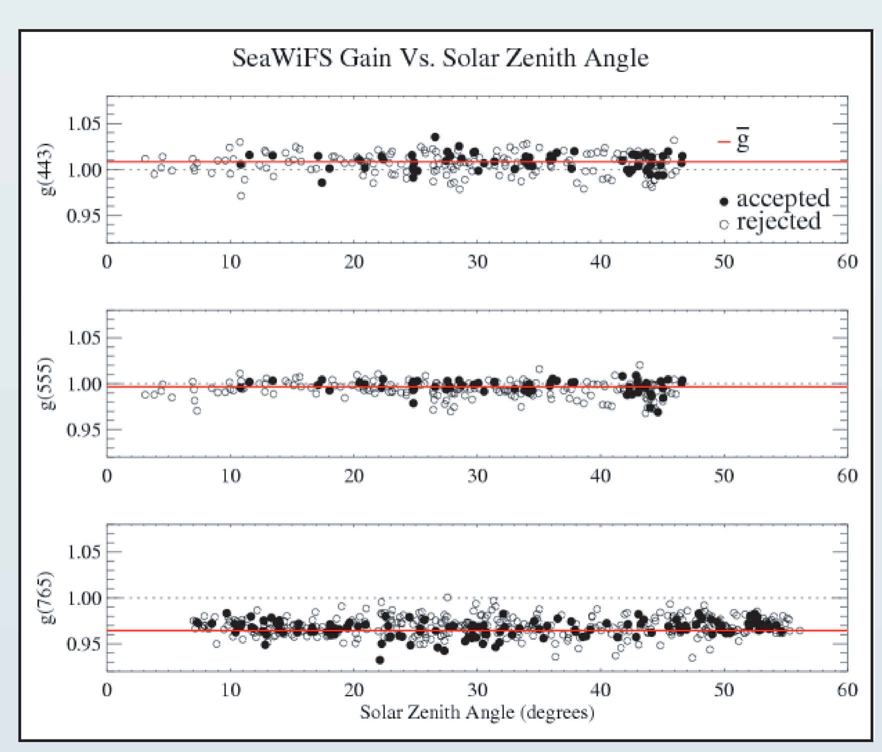


FIGURE 2

For the visible band calibration, cloud and glint-free observations are identified for each target $L_w$(VIS) (recall that the OBPG uses MOBY). The calibrated NIR bands are then used to determine the local aerosol type and concentration, which are subsequently used to estimate $L_a$(VIS).

Using (4) and (5), $L_t$ is predicted and compared with the observed $L_t$ to generate $g$(VIS). As for the NIR, individual g are averaged to determine the mean vicarious gain, $\overline{g}$, for each visible band (Table 2, Figures 1 - 3).

Exclusion criteria are applied to both the satellite and target data. We supplement the satellite quality control metrics of Bailey and Werdell (2006) by limiting valid scenes to those:

(1) with average $C_a$ < 0.25 mg m$^{-3}$
(2) with average aerosol optical thickness at 865-nm < 0.20
(3) without any masked pixels in the 5x5 box

In addition, we visually inspect the surrounding pixels in each scene for undetected clouds and biological and atmospheric homogeneity.

For MOBY, as for all *in situ* targets, we exclude observations with indications of a inhomogeneous water column or cloudy skies.

## COMMENTS

(1) SeaWiFS and MODIS-Aqua $g$ remain relatively stable as a function of time (long-term and seasonally), solar zenith angle, and satellite zenith angle (Figures 1 - 3). The scatter of $g$ (~5% for 443-nm) underscores the need for an independent temporal calibration, as small trends are not detectable here (SeaWiFS 443-nm has degraded ~2% since launch).

SeaWiFS Preliminary Vicarious Gains and Standard Deviations for Reprocessing 6 (Spring 2007)

| | 412 | 443 | 490 | 510 | 555 | 670 | 765 | 865 |
|---|---|---|---|---|---|---|---|---|
| $\overline{g}$ | 1.0324 | 1.0086 | 0.9887 | 0.9955 | 0.9967 | 0.9654 | 0.9645 | 1 |
| $s$ | 0.010 | 0.009 | 0.007 | 0.007 | 0.008 | 0.005 | 0.004 | 0 |

MODIS-Aqua Vicarious Gains and Standard Deviations for Reprocessing 1.1 (August 2005)

| | 412 | 443 | 488 | 531 | 551 | 667 | 678 | 748 | 870 |
|---|---|---|---|---|---|---|---|---|---|
| $\overline{g}$ | 0.9710 | 0.9848 | 0.9795 | 0.9870 | 0.9850 | 0.9797 | 0.9776 | 0.9855 | 1 |
| $s$ | 0.006 | 0.005 | 0.005 | 0.005 | 0.005 | 0.003 | 0.004 | 0.004 | 0 |

SeaWiFS Vicarious Gains, as Above, with the BRDF Correction Disabled ($f_b$ = 1)

| | 412 | 443 | 490 | 510 | 555 | 670 | 765 | 865 |
|---|---|---|---|---|---|---|---|---|
| $\overline{g}$ | 1.0251 | 1.0006 | 0.9803 | 0.9891 | 0.9925 | 0.9643 | 0.9645 | 1 |
| $s$ | 0.007 | 0.008 | 0.007 | 0.007 | 0.007 | 0.005 | 0.004 | |
| % | -1.05 | -1.19 | -1.08 | -0.65 | -0.14 | 0.17 | | |

TABLE 2

(2) SeaWiFS $\overline{g}$ were incorporated into the OBPG validation system and match-up statistics were generated for those observations used in its calculation (Table 3). The satellite-to-*in situ* ratios and biases approach unity and zero, but the absolute median precent differences (MPD) and RMS are not negligible. Note that Bailey and Werdell (2006) report MPD of 13% for SeaWiFS 443-nm for a global, deep water data set.

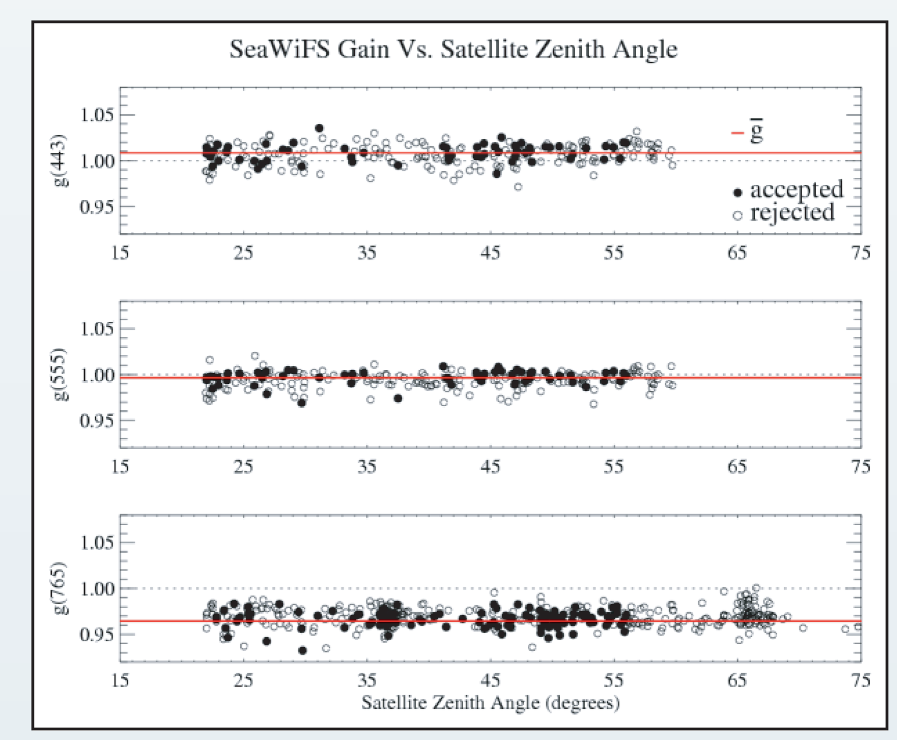


FIGURE 3

(3) The standard errors of $\overline{g}$ reduce to 0.1% as the sample size grows, yet its range (min to max) remains 0.5% (Figure 4). The initial decline in $\overline{g}$ results from the rapid degradation of SeaWiFS in the early part of its mission, where the temporal calibration is least reliable.

Regression Statistics for SeaWiFS "Validation" Using MOBY Calibration Targets

| | 412 | 443 | 490 | 510 | 555 | 670 |
|---|---|---|---|---|---|---|
| N | 60 | 60 | 60 | 60 | 60 | 60 |
| $r^2$ | 0.96 | 0.91 | 0.73 | 0.50 | 0.41 | 0.36 |
| slope | 1.06 | 1.06 | 1.05 | 1.14 | 1.47 | 5.07 |
| intercept | -0.10 | -0.07 | -0.05 | -0.08 | -0.12 | 0.07 |
| RMS | 0.053 | 0.052 | 0.038 | 0.035 | 0.024 | 0.009 |
| bias | 0.02 | 0.02 | 0.01 | 0.01 | 0.00 | 0.00 |
| MPD | 2.1 | 1.9 | 2.2 | 3.1 | 5.4 | 37.2 |
| ratio | 1.008 | 1.011 | 1.009 | 1.010 | 1.003 | 1.081 |

TABLE 3

(4) The OBPG periodically reprocesses the full SeaWiFS record when algorithms are improved or MOBY data are revised. Each reprocessing includes an update to $\overline{g}$. Removing the BRDF correction, for example, changes $\overline{g}$ by ~1% (Table 2). Relative spectral changes in $\overline{g}$ resulting from algorithm uncertainties introduce downstream differences in $C_a$.

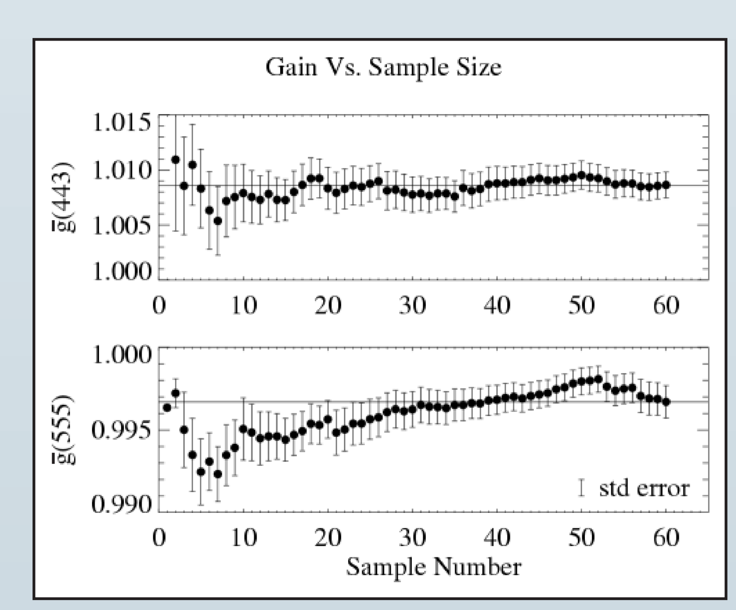


FIGURE 4

Bailey, S.W. and Werdell, P.J., *Rem. Sens. Environ.*, 102, 12-23, 2006.
Clark, D.K. and 5 co-authors, *J. Geophys. Res.*, 102, 17209-17217, 1997.
Eplee Jr., R.E. and 7 co-authors, *Appl. Opt.*, 40, 6701-6718, 2001.
Gordon, H.R., *Rem. Sens. Environ.*, 63, 265-278, 1998.
Gordon, H.R. and Wang, M., *Appl. Opt.*, 33, 443-452, 1994.